Original Research

Highly stable carbon-coated nZVI composite Fe^0@RF-C for efficient degradation of emerging contaminants

Guizhou Xu [a], Lin Sun [a], Yizhou Tu [a], Xiaolei Teng [a], Yumeng Qi [a], Yaoyao Wang [a], Aimin Li [a], Xianchuan Xie [b, c, d, *], Xueyuan Gu [a, **]

[a] State Key Laboratory of Pollution Control and Resource Reuse, School of the Environment, Nanjing University, Nanjing, 210023, China
[b] Key Laboratory of Poyang Lake Environment and Resource Utilization, Engineering Research Center of Watershed Carbon Neutralization, Ministry of Education, School of Resource and Environment, Nanchang University, Nanchang, 330031, China
[c] Nanjing University & Yancheng Academy of Environment Protection Technology and Engineering, Nanjing, 210023, China
[d] Jiangxi Nanxin Environmental Protection Technology Co. LTD, Jiujiang City, Jiangxi Province, 330300, China

ARTICLE INFO

ABSTRACT

Nanoscale zerovalent iron (nZVI) has garnered significant attention as an efficient advanced oxidation activator, but its practical application is hindered by aggregation and oxidation. Coating nZVI with carbon can effectively addresses these issues. A simple and scalable production method for carbon-coated nZVI composite is highly desirable. The anti-oxidation and catalytic performance of carbon-coated nZVI composite merit in-depth research. In this study, a highly stable carbon-coated core-shell nZVI composite (Fe^0@RF-C) was successfully prepared using a simple method combining phenolic resin embedding and carbothermal reduction. Fe^0@RF-C was employed as a heterogeneous persulfate (PS) activator for degrading 2,4-dihydroxybenzophenone (BP-1), an emerging contaminant. Compared to commercial nZVI, Fe^0@RF-C exhibited superior PS activation performance and oxidation resistance. Nearly 95% of BP-1 was removed within 10 min in the Fe^0@RF-C/PS system. The carbon layer promotes the enrichment of BP-1 and accelerates its degradation through singlet oxygen oxidation and direct electron transfer processes. This study provides a straightforward approach for designing highly stable carbon-coated nZVI composite and elucidates the enhanced catalytic performance mechanism by carbon layers.

1. Introduction

Zerovalent iron (ZVI) has attracted extensive attention in environmental remediation due to its environmental friendliness, low cost, and high reactivity [1,2]. ZVI can be directly used for the reduction of pollutants such as heavy metals [3], nitro compounds [4,5], halides [6–8], and other pollutants readily accept electrons. For pollutants that do not readily accept electrons, such as phenols, ZVI can also be used as an activator of persulfate (PS) and H$_2$O$_2$ to oxidize them [9,10].

Nanoscale ZVI (nZVI) has a higher specific surface area and reduction activity than commonly used microscale ZVI. However, in practical application, nZVI is prone to aggregation and oxidation by air, seriously affecting its performance [11–14]. Many porous materials, such as resin [15], activated carbon [16], biochar [17], and carbon nanotubes [18], have been used as supports for nZVI to promote its dispersion. However, the nZVI particles are exposed on the surface of these supports, which makes it difficult to effectively solve the problem of air oxidation [11,14]. Recent studies have found that encapsulating nZVI into porous carbon materials can significantly improve air stability [11–14]. Hydrothermal carbonization combined with carbothermal reduction is the most used method to prepare carbon-coated nZVI composites [12,14]. The nZVI precursor (iron salts or iron oxides) first undergoes a hydrothermal reaction with a glucose solution. The resulting residue is subjected to high-temperature carbothermal reduction under an inert gas atmosphere to obtain carbon-coated nZVI composites. This method has several drawbacks, including a long hydrothermal

reaction time (10−18 h), high temperatures (typically 180 °C), and pressurized hydrothermal equipment, which poses safety risks and is not conducive to large-scale production. In addition, as mentioned above, ZVI can be used as an activator of PS to degrade pollutants. However, most current studies on carbon-coated nZVI composites mainly focus on improving nZVI oxidation resistance by the carbon layer, with few studies investigating its role in activating PS to enhance pollutant degradation. Moreover, apart from indicating that the carbon layer adsorbs and concentrates pollutants, there is a lack of research on how it enhances pollutant degradation. Therefore, it is necessary to develop a simpler method for preparing carbon-coated nZVI composites that can be easily scaled up for production and systematically study the influence of carbon layers on the catalytic performance of nZVI composites.

As a typical benzophenone-type ultraviolet (UV) filter, 2,4-dihydroxybenzophenone (BP-1) is widely utilized in pharmaceuticals and personal care products [19]. Due to its extensive use, BP-1 has been detected in different water bodies and human urine, blood, and milk [20−24]. For example, the concentration of BP-1 in surface waters ranged from 4.22 to 19.4 ng L^{-1} [19], while the mean concentration of BP-1 in the effluent in Hong Kong is as high as 163 ng L^{-1} [25]. Many studies have shown that BP-1 has endocrine-disrupting and carcinogenic effects [26−28], which pose potential risks to the ecological environment and human health. Unfortunately, it is difficult to completely remove BP-1 using conventional methods in wastewater treatment plants [25]. In recent years, an advanced oxidation process (AOP) based on hydroxyl or sulfate radicals has been widely used to oxidize various refractory organic pollutants [9,29−34]. The activation of PS by nZVI is an effective way to produce hydroxyl and sulfate radicals. Given the carbon layer on carbon-coated nZVI composite enhances nZVI stability and pollutant absorption, the high degradation efficiency of BP-1 is anticipated when activating PS with this composite.

Phenolic resin has a high carbon content, which can generate many pores during high-temperature carbonization. Fe_3O_4 is cheap and can be reduced to ZVI by carbon at high temperatures. Therefore, phenolic resin and Fe_3O_4 are ideal carbon and iron sources for preparing carbon-coated ZVI composites. In this study, spheroidal nano-Fe_3O_4 was firstly coated with resorcinol-formaldehyde (RF) resin under mild conditions, then a stable carbon-coated core-shell nZVI composite, Fe^0@RF-C was successfully prepared through carbothermal reduction under the protection of N_2. The degradation of BP-1 in the Fe^0@RF-C/PS system was systematically investigated. In addition, the activation mechanism of Fe^0@RF-C on PS was explored, based on which the important role of the carbon layer in improving the catalytic performance of Fe^0@RF-C was discussed. Finally, possible degradation pathways of BP-1 were proposed, and the toxicity changes during the degradation process were evaluated using the ecological structure-activity relationship (ECOSAR) program. This study provides a simple, feasible scheme for preparing stable carbon-coated core-shell nZVI composite. It elucidates the important role of the carbon layer on the catalytic performance of nZVI composites and its underlying mechanism. These findings significant for applying nZVI and removing refractory organic matter in water.

2. Material and methods

2.1. Chemicals and materials

All chemicals and materials used in this study are presented in the Supporting Information (Supplementary Material Text S1).

2.2. Fe^0@RF-C preparation

The Fe^0@RF-C composite was prepared by calcining pre-synthesized RF resin coated magnetite particles (Fe_3O_4/RF) under N_2. Specifically, 2.5 g resorcinol was fully dissolved in 20 mL ethanol and 50 mL water. Then, 1.25 g Fe_3O_4 nanoparticles were added to the solution and fully dispersed by ultra-sonication. In the resultant dispersion, 1.25 mL of ammonia was added, followed by 3.5 mL of formaldehyde, and the mixture was mechanically stirred for 1 h at 200−300 rpm and 30 °C. After magnetic separation, the solid particles were washed three times with deionized water and then vacuum dried at 80 °C for 12 h to obtain Fe_3O_4/RF particles. Subsequently, the Fe_3O_4/RF particles were calcined under a N_2 atmosphere at 400 °C for 3 h, followed by further treatment at 850 °C for 3 h at a heating rate of 5 °C min^{-1}. Carbon derived from the formaldehyde resin (RF-C) without adding Fe_3O_4 was also synthesized for comparison.

2.3. Characterization

The characterization of Fe^0@RF-C is presented in Text S2 (Supplementary Material).

2.4. Experimental procedures

Batch oxidation reactions of BP-1 were carried out in 250 mL conical flasks in a water bath at 25 °C. In a typical experiment, 5 mg of Fe^0@RF-C was fully dispersed in 100 mL of BP-1 solution (20 μmol L^{-1}) with an initial pH of 5.0 ± 0.1 (adjusted with 0.1 mol L^{-1} H_2SO_4 and 0.1 mol L^{-1} NaOH) under stirring (200−300 rpm). After that, 100 μL of PS solution (1 mol L^{-1}) was added to the mixture to initiate the oxidation reaction. At given intervals, 1 mL of the reaction solution was withdrawn and immediately quenched with 1 mL of methanol. After filtered through a polytetrafluoroethylene (PTFE) membrane, the concentration of BP-1 in the sample was analyzed using high-performance liquid chromatography (HPLC). In addition, the effects of the catalyst dosages, initial solution pH, [PS]:[BP-1] ratios, humic acid (HA) concentrations, common inorganic ions, and water matrices (including ultrapure water (UP), tap water (TW), secondary clarifier effluent (SCE), synthetic wastewater (SW) and river water (RW)) on the degradation of BP-1 were also studied. The water matrices are detailed in Text S3 (Supplementary Material), and the water parameters are listed in Table S1 (Supplementary Material). Quenching experiments were conducted with methanol (MeOH), tert-butanol (TBA), superoxide dismutase (SOD), furfuryl alcohol (FFA), 2,2,6,6-tetramethyl-4-piperidinol (TEMP), L–Histidine (L-his), and sodium azide (NaN$_3$) as quenching agents, respectively. All experiments were duplicated, and the results were presented as mean data with standard deviations.

2.5. Analytical methods

The concentration of BP-1 was determined by an Agilent 1260 HPLC (Agilent Technologies, USA). The degradation intermediates were analyzed using an Agilent 1260 HPLC system in tandem with a high-resolution hybrid quadrupole time-of-flight mass spectrometer (Triple TOF 5600, AB Sciex, Foster City, CA) equipped with an electrospray for electrospray ionization (ESI) in negative ion mode. The HPLC and HPLC-mass spectrometry/mass spectrometry (HPLC-MS/MS) parameters are described in Text S4 and Text S5 (Supplementary Materials). Before analysis, all the degradation intermediates were enriched through solid phase extraction (SPE)

using CNWBOND LC-C18 SPE cartridges (1 g, 6 mL, CNW Technologies, Shanghai, China) conducted on an automatic solid phase extraction instrument (Trace 280, Thermometer). The SPE operation procedure is described in detail in Text S6 (Supplementary Material).

The reaction solution's total organic carbon (TOC) was determined during the oxidation process using a TOC analyzer (multi N/C 3100, Analytik Jena). The concentration of PS was measured using a UV−Vis spectrophotometer (SPECORD 210, Analytik Jena) based on the method of Liang et al. [35]. The reactive oxygen species (ROS) generated in the oxidation system were detected using the EMX PLUS spectrometer (Bruker BioSpin, Germany) with 5, 5-dimethyl-1-pyrroline N-oxide (DMPO) and TEMP as spin-trapping reagents.

2.6. Electrochemical measurements

The electrochemical tests were conducted in 100 mmol L^{-1} phosphate buffer solution (pH 7) using an electrochemical workstation with a standard three-electrode configuration (CH1760E, Beijing Huakeputian Technology Co., Ltd.). The Ag/AgCl/KCl electrode, platinum wire electrode, and an activator-coated glassy carbon electrode were used as the reference, counter, and working electrode. 10 mg of activator, 2 mL of ethanol and water mixture (v:v = 1:1), and 10 μL of Nafion perfluorinated resin solution (5 wt%, 3A materials) were sonicated for 1 h. Then, the mixture (5 μL) was dropped onto a glassy carbon electrode and dried for 10 min at 60 °C. The above procedure was repeated three times. Amperometric $i−t$ curves were measured by applying a potential of +0.6 V (vs Ag/AgCl) to the working electrode.

2.7. Toxicity assessment

The acute and chronic toxicity of BP-1 and its oxidation intermediates to three typical aquatic organisms (i.e., fish, daphnia, and green algae) were evaluated using the ECOSAR program, which has been widely used for toxicity prediction by the United States Environmental Protection Agency (US EPA), Organization for Economic Co-operation and Development (OECD), and the European Union (EU) [19,29]. Toxicity was assessed regarding the half-lethal concentration (LC$_{50}$) for daphnia and fish and the half-effective concentration (EC$_{50}$) for green algae, with smaller values indicating higher toxicity.

3. Results and discussion

3.1. Characterization of Fe^0@RF-C

3.1.1. Morphology characterization

RF-C comprises irregular particles with distinct stacking pores (Fig. 1a). The Fe$_3$O$_4$ particles primarily occurred as smooth spheroids with sizes ranging from a few hundred nanometers to two microns (Fig. 1b). After carbon coating, the prepared Fe^0@RF-C composites maintained the spherical morphology with rougher surface, which was reflected by the broken particles in the scanning electron microscopy (SEM) images (Fig. 1c). Energy-dispersive X-ray spectroscopy (EDS) mapping (Fig. 1d) revealed that almost all Fe^0@RF-C composites were coated with a layer of carbon. In the high-resolution transmission electron microscopy (HTEM) image (Fig. 1e), a core-shell structure of Fe^0@RF-C composites with a coating of approximately 20 nm thick can be observed. The lattice fringes with a spacing of approximately 0.36 nm in the carbon coating layer, which is assigned to the (002) plane of graphitic carbon, can be observed (Fig. 1f), indicating that the carbon layer was partly graphitized [36]. Many researchers have reported that graphitic carbon has excellent charge transfer performance, which
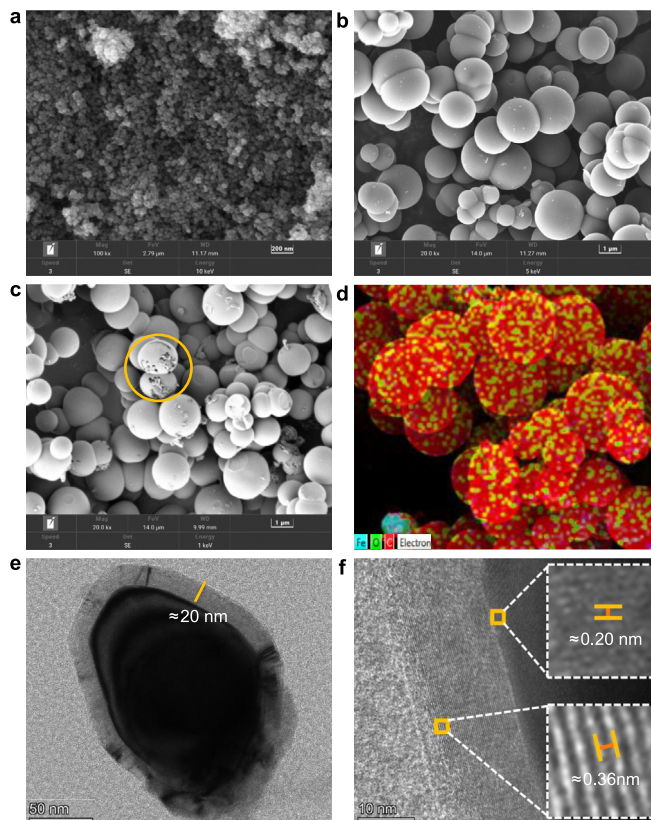
Fig. 1. a−c, SEM images of RF-C (**a**), raw Fe$_3$O$_4$ particles (**b**), and Fe^0@RF-C particles (**c**). **d**, EDS mapping images of Fe^0@RF-C particles. **e−f**, HRTEM images of Fe^0@RF-C particles at 50 nm (**e**) and 10 nm (**f**) scales.

is beneficial to the oxidation of pollutants [37−40]. In addition, lattice fringes with a spacing of about 0.20 nm can also be observed in the iron core, which is attributable to the (110) plane of crystalline Fe^0 [36].

3.1.2. Compositional characterization

The diffraction patterns of the Fe^0@RF-C composites were well consistent with the standard X-ray diffraction (XRD) patterns of Fe^0 (JCPDS 99−0064) with diffraction peaks at 2θ of 44.9°, 65.3°, and 82.5° (Fig. 2a) [14]. The characteristic diffraction patterns of Fe$_3$O$_4$ were not detected in Fe^0@RF-C, indicating that the Fe$_3$O$_4$ was completely reduced into Fe^0 during the calcination. Moreover, an obvious diffraction peak at 2θ of 26.3° was observed, which was attributed to the (002) plane of graphitic carbon (JCPDS 26−1080) [36].

The intensity of the Fe 2p X-ray photoelectron spectroscopy (XPS) spectra is very weak (Fig. 2b), indicating low iron content on the surface, which further confirms that the iron species are closely wrapped by graphitic carbon layers. Two major peaks corresponding to Fe 2p3/2 and Fe 2p1/2 with binding energies at 710.5 and 723.6 eV were detected, characteristic of Fe$_3$O$_4$ [41]. The Fe^0 peak, which often appears at 707.2 eV [42], was not detected, which could be attributed to the superficial oxidation of Fe^0 upon exposure to air.

The Raman spectra were determined to investigate the state of carbon in Fe^0@RF-C (Fig. 2c). Two distinct characteristic peaks were observed at 1350 and 1580 cm^{-1}, corresponding to the D and G bands, respectively. The D band was associated with disordered carbon, while the G band was attributed to in-plane vibrations of the sp^2 carbon [17]. The ratios of band intensity of the D band to G
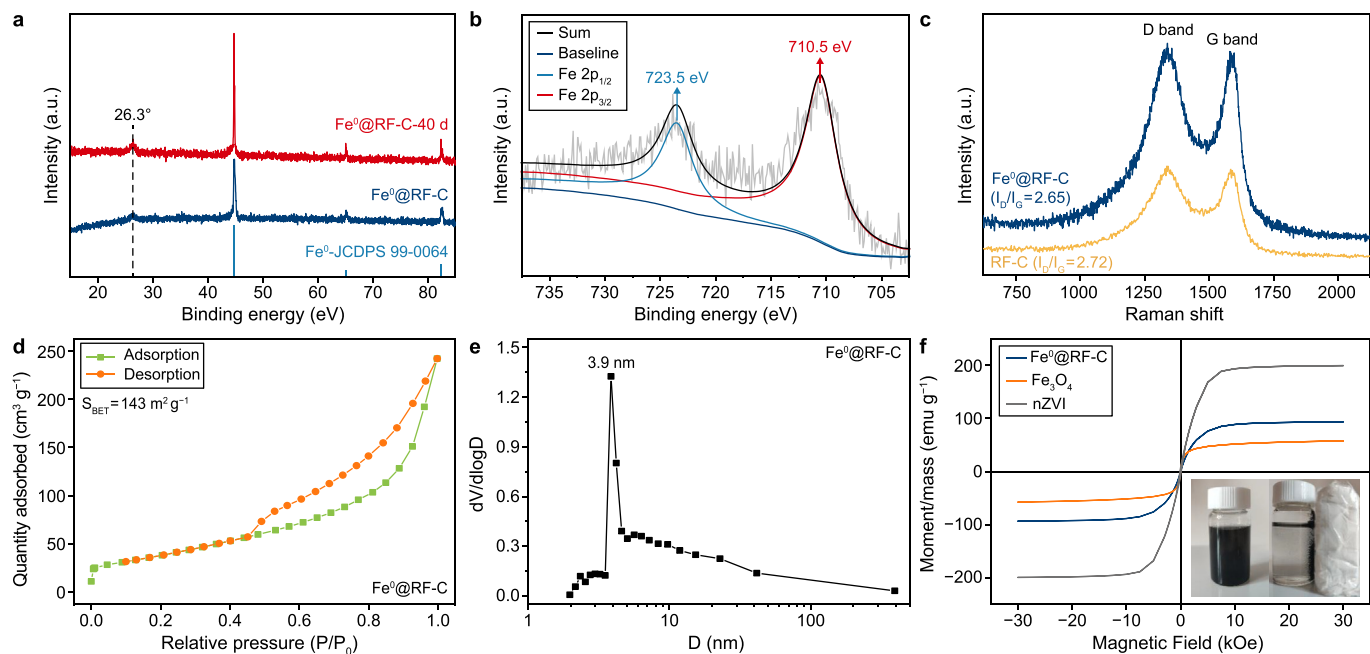
Fig. 2. a, XRD pattern. **b**, High-resolution XPS spectra of Fe 2p. **c**, Raman spectra. **d**, N$_2$ adsorption-desorption isotherm. **e**–**f**, Pore distribution (**e**), and magnetic hysteresis loop (**f**) of Fe^0@RF-C.

band (I$_D$/I$_G$), which reflect the degree of graphitization [43], were 2.65 and 2.72 for Fe^0@RF-C and RF-C respectively, indicating that the carbon layer was partly graphitized.

Considering the results of SEM, HTEM, EDS mapping, XRD, XPS, and Raman spectra, a core-shell structure with a Fe^0 core and partially graphitized carbon coating of Fe^0@RF-C can be verified.

3.1.3. Pore structure characterization

The N$_2$ adsorption-desorption isotherm of Fe^0@RF-C composites exhibited a clear hysteresis loop within the relative pressure range of P/P$_0$ = 0.4–1.0, characteristic of large mesopores (Fig. 2d) [44]. Based on the Brunauer-Emmett-Teller (BET) model, the specific surface area (S$_{BET}$) of Fe^0@RF-C was calculated to be 143 m^2 g^{-1}. The plot of pore size distribution, determined from the desorption branch based on the Barrett-Joyner-Halenda (BJH) method, exhibited obvious mesopores centered at 3.9 nm (Fig. 2e). For comparison, the N$_2$ adsorption-desorption isotherms and pore size distributions of RF-C and raw material Fe$_3$O$_4$ were also plotted (Supplementary Material Fig. S1). RF-C exhibited a type I isotherm in the low-pressure region (P/P$_0$ < 0.4) without any hysteresis loop (Supplementary Material Fig. S1a), indicating its microporous structure [43]. The S$_{BET}$ of RF-C was 491 m^2 g^{-1}. The pore size distribution of RF-C was concentrated at approximately 2.2 nm (Supplementary Material Fig. S1b). A hysteresis loop was also observed in the isotherm of Fe$_3$O$_4$ (Supplementary Material Fig. S1c), which is attributed to the stacking of pores. The S$_{BET}$ of Fe$_3$O$_4$ is 101 m^2 g^{-1}, and a wide pore size distribution centered at approximately 10.4 nm could be observed (Supplementary Material Fig. S1d). The significant decrease of S$_{BET}$ for Fe^0@RF-C compared with RF-C is attributable to the large amount of nonporous Fe^0 in the composites. Based on the combustion method, the mass fraction of Fe^0 in Fe^0@RF-C was 54.9%.

3.1.4. Magnetic characterization

The magnetic properties of commercial Fe$_3$O$_4$, nZVI, and Fe^0@RF-C were evaluated for comparison (Fig. 2f). All the samples corresponded to the typical S-type magnetic hysteresis loop with no remanence or coercivity at room temperature, indicating superparamagnetic behavior [43]. The saturation magnetization (Ms) of Fe^0@RF-C, Fe$_3$O$_4$, and nZVI were 93.43, 57.56, and 199.34 emu g^{-1}, respectively. Therefore, Fe^0@RF-C has a lower magnetism than nZVI, which may be attributed to the carbon layer on Fe^0@RF-C. A similar phenomenon has been reported in the composites of nZVI and activated carbon (AC-nZVI) [45]. In addition, although the magnetism of Fe^0@RF-C was weaker than that of nZVI, it could be easily separated by an external magnetic field after dispersion in water (insert in Fig. 2f), which is beneficial for its practical application.
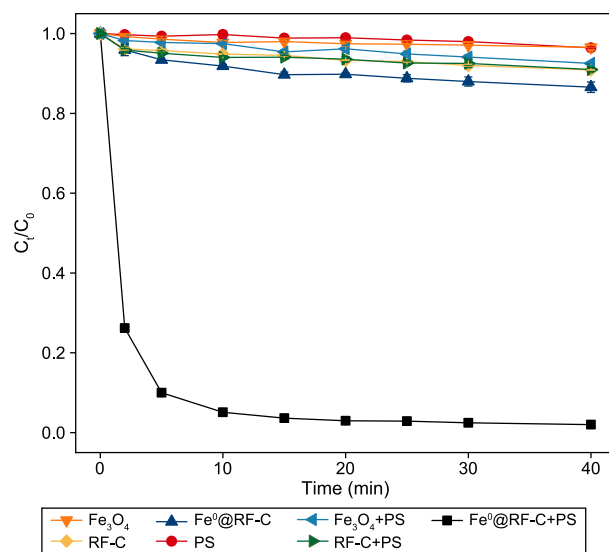
Fig. 3. Removal of BP-1 under different oxidation systems. Typical reaction conditions: [BP-1] = 20.0 μmol L^{-1}, [BP-1]:[PS] = 1:50, catalyst dosage = 50 mg L^{-1}, initial solution pH = 5.0 ± 0.1, T = 25.0 °C.

3.2. BP-1 degradation by PS activated with Fe⁰@RF-C

3.2.1. Evaluation of catalytic performance of Fe⁰@RF-C

In separate systems with only $Fe^0@RF-C$, Fe_3O_4, and RF-C, 13.4%, 3.4%, and 9.1% of BP-1 were removed after 40 min, respectively (Fig. 3), indicating that adsorption contributed little to the removal of BP-1. For a sole-PS system, the removal efficiency of BP-1 was only 3.6% after reacting for 40 min, indicating that the direct oxidation of BP-1 by PS was negligible at room temperature. Neither RF-C nor Fe_3O_4 could effectively activate PS because the removal efficiencies of BP-1 after 40 min in the RF-C/PS and Fe_3O_4/PS systems were only 9.0% and 7.5%, respectively. The ineffective PS activation performance of Fe_3O_4 was also reported in an early study for the degradation of 4-chlorophenol [14]. In contrast, the removal efficiency of BP-1 in the $Fe^0@RF-C$/PS system significantly increased to 94.9% in only 10 min, suggesting that PS was efficiently activated by $Fe^0@RF-C$. Therefore, it can be concluded that in a mixed PS and $Fe^0@RF-C$ system, neither the direct oxidation of PS nor adsorption by $Fe^0@RF-C$ dominates the removal of BP-1. Instead, the removal of BP-1 is primarily facilitated by the catalytic oxidation of PS activated by $Fe^0@RF-C$. Similar results have been reported for BP-1 degradation in a Fe^0/PS system, but the degradation rate of BP-1 is faster in the $Fe^0@RF-C$/PS system in this study [29]. The removal of BP-1 under different systems approximately obeys the pseudo-first-order kinetics model (Supplementary Material Fig. S2). The kinetics constant (k_{obs}) of BP-1 removal in $Fe^0@RF-C$/PS system was calculated as 0.4892 min⁻¹, which is much higher than that in PS (0.0007 min⁻¹), $Fe^0@RF-C$ (0.0046 min⁻¹), Fe_3O_4 (0.0010 min⁻¹), RF-C (0.0029 min⁻¹), Fe_3O_4/PS (0.0021 min⁻¹), RF-C/PS (0.0029 min⁻¹) systems.

The adsorption of organics by carbon materials has been reported to have a positive synergistic effect on the following advanced oxidation process [46,47]. In addition, the graphitized structure was crucial to the electron transfer on the surface of carbon materials [16,40,48,49]. Therefore, the outstanding oxidative degradation performance of the $Fe^0@RF-C$/PS system for BP-1 can be explained as follows. The porous structure of the carbon layer on the surface of $Fe^0@RF-C$ is conducive to the adsorption of BP-1 (13.4% of BP-1 was adsorbed in the sole-$Fe^0@RF-C$ system), which increases the concentration of BP-1 on the surface and shortens the distance between BP-1 and the generated free radicals (described in section 3.3), thus enhancing the degradation of BP-1. The adsorption and oxidation of BP-1 play a synergistic role in its removal process; that is, adsorption can promote oxidation; similarly, after the adsorbed BP-1 is oxidized, $Fe^0@RF-C$ can continue to adsorb BP-1. In addition, the graphitized carbon layer may also act as an electron transfer medium from BP-1 to PS (described in section 3.3), further improving the degradation efficiency of BP-1.

3.2.2. Stability of Fe⁰@RF-C

$Fe^0@RF-C$ and commercial nZVI (50 nm, sphere) were exposed to air for 40 days to estimate the stability of $Fe^0@RF-C$. After five days ($Fe^0@RF-C$-5 d and nZVI-5 d) and 40 days ($Fe^0@RF-C$-40 d and nZVI-40 d) of exposure, $Fe^0@RF-C$ and nZVI were taken for BP-1 degradation experiments. The fresh $Fe^0@RF-C$ presented excellent PS activation performance, with more than 90% degradation efficiency of BP-1 in 5 min (Fig. 4a). Although the activation performance of $Fe^0@RF-C$-5 d and $Fe^0@RF-C$-40 d slightly declined, more than 90% of BP-1 could be degraded in 10 min, indicating the high stability of $Fe^0@RF-C$. The stability of $Fe^0@RF-C$ was also confirmed by XRD characterization, which showed that the material still exists in the state of Fe^0 after exposure to air for 40 days (Fig. 2a). The improvement of Fe^0 stability by carbon coating has also been reported by many other studies [13,14]. Fresh commercial nZVI showed good PS activation performance, with over 80% of BP-1
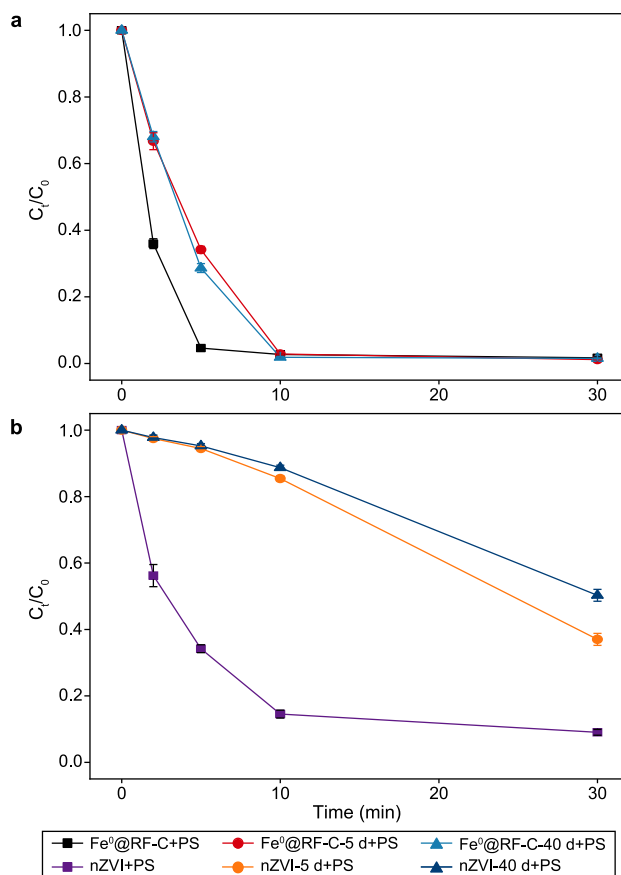

Fig. 4. Degradation of BP-1 in PS systems using $Fe^0@RF-C$ (**a**) and commercial nZVI (**b**) exposed to air for different days as activators.

degraded in 10 min (Fig. 4b). However, the performance of nZVI-5 d and nZVI-40 d substantially declined, reflecting the susceptibility of nZVI to oxidize in the atmosphere. The pseudo-first-order kinetics model further fitted the removal of BP-1 under different systems (Supplementary Material Fig. S3). The k_{obs} values of BP-1 removal in PS systems activated by $Fe^0@RF-C$, $Fe^0@RF-C$-5 d, and $Fe^0@RF-C$-40 d were calculated as 0.6002, 0.2131, and 0.2421 min⁻¹, respectively. For comparison, the k_{obs} values of BP-1 removal in PS systems activated by nZVI, nZVI-5 d, and nZVI-40 d were only 0.1948, 0.0148, and 0.0115 min⁻¹, respectively. Even after 40 days of air exposure, $Fe^0@RF-C$ showed better PS activation performance than commercial nZVI. These results indicate that the oxidation of Fe^0 was significantly slowed down in $Fe^0@RF-C$, which can be attributed to the coating of the carbon layer [14,36,43,50].

3.2.3. Effect of catalyst dosage and PS concentration

The removal kinetics of BP-1 accelerates with the increase of $Fe^0@RF-C$ dosage in the range of 10−100 mg L⁻¹ (Fig. 5a). Additionally, BP-1 removal approximately followed by the pseudo-first-order kinetics model and the k_{obs} value increased from 0.3317 to 0.4973 min⁻¹ with the $Fe^0@RF-C$ dosage increased from 10 to 100 mg L⁻¹ (Supplementary Material Fig. S4a). After 10 min of reaction, the removal efficiencies of BP-1 exceeded 94.0% and reached their maximum for all the studied $Fe^0@RF-C$ dosages. The $Fe^0@RF-C$ dosage was set as 50 mg L⁻¹ in the following experiments for convenience. It is worth mentioning that the dosage of $Fe^0@RF-C$ used in this study is very low compared with other reported iron-based catalysts for PS activation, usually ranging from 200 to 1000 mg L⁻¹ [14,16,18,51].
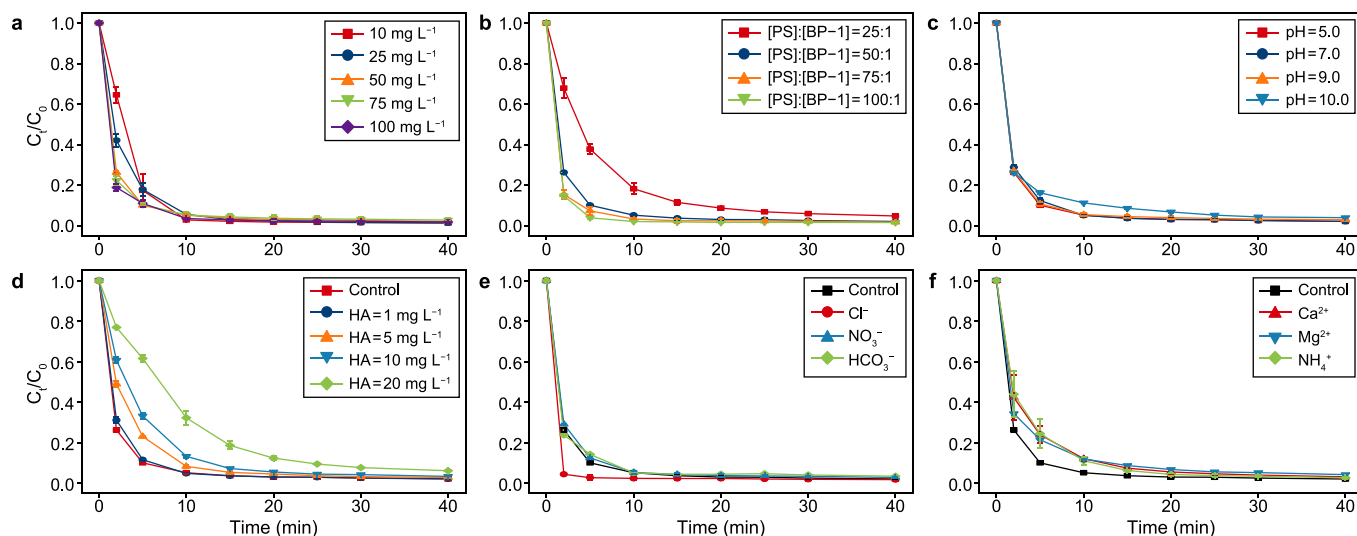
Fig. 5. Effects of catalyst dosage (**a**), PS concentration (**b**), initial solution pH (**c**), HA concentration (**d**), and coexisting anions (**e**) and cations (**f**) on the degradation of BP-1. Typical reaction conditions: [BP-1] = 20.0 μmol L^{-1}, [BP-1]:[PS] = 1:50, catalyst dosage = 50 mg L^{-1}, initial solution pH = 5.0 ± 0.1, T = 25.0 °C.

The increase in the ratios of PS to BP-1 from 25:1 to 50:1 resulted in a significant improvement in the degradation efficiency of BP-1 (Fig. 5b). The improvement became less prominent with further increases in PS concentration. The removal efficiencies of BP-1 at all PS concentrations exceeded 90.0% after 20 min. Additionally, BP-1 removal approximately obeys the pseudo-first-order kinetics model, and the k_{obs} value increased from 0.1948 to 0.6964 min^{-1} when the molar ratio of PS to BP-1 increased from 25:1 to 100:1 (Supplementary Material Fig. S4b). According to previous studies [29,52–54], excessive addition of PS may lead to the consumption of the generated free radicals, which is detrimental to the oxidation of pollutants. However, this phenomenon was not observed in this study, which may be related to the multiple degradation mechanisms of BP-1 in the system (see discussion in Section 3.3). Considering the efficiency and economic advantages, the molar ratio of PS to BP-1 was set as 50:1 in the following experiments, which is much lower than those reported in most PS-based advanced oxidation processes with the molar ratios of PS to pollutants from 100:1 to 500:1 [16,29,37,55,56].

3.2.4. Effects of initial solution pH, HA, and coexisting ions

The degradation of BP-1 was almost unaffected by the initial solution pH, except that the degradation of BP-1 was slightly inhibited when the initial solution pH was 10.0 (Fig. 5c). After reacting for 30 min, the degradation efficiency of BP-1 reached more than 95% for all experiments. Additionally, BP-1 removal approximately obeys the pseudo-first-order kinetics model, and the k_{obs} value slightly decreased from 0.4892 to 0.4070 min^{-1} when the initial solution pH increased from 5.0 to 10.0 (Supplementary Material Fig. S4c). The final solution pH after reactions was also measured, all below 3.1 (Supplementary Material Table S2). Under acidic conditions, Fe^0 in Fe^0@RF-C was easily corroded to generate Fe^{2+}, an effective homogeneous catalyst for PS activation, leading to rapid degradation of BP-1.

HA was selected as a representative to investigate the effect of natural organic matter on the degradation of BP-1 (Fig. 5d). At a low HA concentration of 1 mg L^{-1}, the degradation efficiency of BP-1 was almost unaffected. However, the degradation efficiencies of BP-1 decreased with further increasing HA concentrations. In addition, BP-1 removal approximately obeys the pseudo-first-order kinetics model, and the k_{obs} value greatly decreased from 0.4892 to 0.1018 min^{-1} when the HA concentration increased from 0 to 20 mg L^{-1} (Supplementary Material Fig. S4d). The negative effect of HA on the PS-based oxidation systems has also been reported by many studies and can be explained by the competitive reactions between HA and pollutants [55,57]. Moreover, although HA showed an inhibitory effect on the degradation of BP-1, 93.9% of BP-1 could still be degraded after 40 min at a high HA concentration of 20 mg L^{-1}. Thus, the Fe^0@RF-C/PS system strongly resists natural organic matter interference in practical applications.

The effects of coexisting ions on the degradation of BP-1 were studied at an ion concentration of 5.0 mmol L^{-1}. According to the literature, Cl$^-$ has different effects on the degradation of pollutants in different oxidation systems. Generally, the presence of Cl$^-$ inhibits pollutant degradation due to its scavenging effect on HO$^\bullet$ and SO$_4^{\bullet-}$ [58–60]. However, in this study, the presence of Cl$^-$ significantly promoted the degradation of BP-1 (Fig. 5e). In fact, the promotion of Cl$^-$ to the degradation of pollutants has also been reported in many oxidation processes and it is generally believed that the possible reason is due to the formation of various chlorine-containing radicals (Cl$^\bullet$ and Cl$_2^{\bullet-}$) and free available chlorine (Cl$_2$) [61–63]. The presence of HCO$_3^-$ and NO$_3^-$ showed no clear effect on the degradation of BP-1. Ca^{2+}, Mg^{2+}, and NH$_4^+$ showed similar and very weak inhibition effects on the degradation of BP-1, but the degradation efficiency of BP-1 all exceeded 90.0% in about 15 min (Fig. 5f). The removal of BP-1 under different coexisting ions was then fitted by the pseudo-first-order kinetics model (Supplementary Material Figs. S4e–f). The k_{obs} values of BP-1 removal in the presence of Cl$^-$, NO$_3^-$, HCO$_3^-$, Ca^{2+}, Mg^{2+}, and NH$_4^+$ were calculated as 0.8424, 0.4448, 0.4358, 0.2947, 0.3276, and 0.2876 min^{-1}, respectively. The above results show that the Fe^0@RF-C/PS system has excellent resistance to interference from ions.

3.2.5. The residual PS concentration and leakage of iron ions

The concentration of PS rapidly decreased to approximately 60% in the first 5 min, after which it gradually decreased (Supplementary Material Fig. S5a), indicating that Fe^0@RF-C has high activation performance for PS. It should be noted that nearly 30% of PS remained after 40 min, indicating excessive PS in the system. In the system without PS and BP-1, the iron ion concentration was only 0.4 mg L^{-1} after 40 min (Supplementary Material

Fig. S5b), indicating the stability of Fe⁰@RF-C in water. In the Fe⁰@RF-C/PS/BP-1 mixed system, the iron ion concentration rapidly increased after adding PS. After 40 min, the iron ion concentration reached 12.6 mg L⁻¹. Furthermore, we found that in the mixed system of Fe⁰@RF-C/PS without adding BP-1, the dissolution of iron was less than that in the mixed system of Fe⁰@RF-C/PS/BP-1. This is because the addition of BP-1 leads to the consumption of $SO_4^{\bullet-}$, which in turn promotes the reaction between Fe⁰ and PS, producing more iron ions.

3.2.6. Removal of BP-1 in different water matrices

Considering the complexity of water matrices in practical application, BP-1 degradation experiments were conducted in different types of water matrices (Supplementary Material Fig. S6). BP-1 was rapidly degraded in UP, with the degradation efficiency reaching 94.9% in 10 min. Unexpectedly, the degradation of BP-1 was almost unaffected in TW, SCE, and RW, but it was slightly inhibited in SW. The degradation efficiencies of BP-1 exceeded 90% after 10 min in all water matrices. These results differ from previous reports that water matrices significantly influence the degradation of BP-1 in the Fe⁰/PS system [29]. In their studies, Cl⁻ in TP and SCE promoted the degradation of BP-1, while organic matter in RW and SW inhibited the degradation of BP-1. In this study, the influence of different water matrices on the degradation of BP-1 was not significant, which may be related to the different degradation mechanisms of BP-1 in the Fe⁰@RF-C/PS system (described in section 3.3).

3.3. Activation mechanism of PS with Fe⁰@RF-C

To identify the types of reactive species generated in the Fe⁰@RF-C/PS system, electron paramagnetic resonance (EPR) experiments using DMPO and TEMP as spin-trapping agents for radicals and singlet oxygen ($^1O_2$) were conducted first. The detections of $SO_4^{\bullet-}$, HO• and $^1O_2$ were performed in the water system, while for $O_2^{\bullet-}$, it was conducted in the MeOH system [64]. No free radical signal is recorded in the DMPO system alone (Fig. 6a). Weak signals of HO• are observed in the mixed system of Fe⁰@RF-C and DMPO, which may be attributable to the reaction of Fe⁰ with H_2O and dissolved O_2 [14,65]. Both $SO_4^{\bullet-}$ and HO• signals are detected in the PS/DMPO and Fe⁰@RF-C/PS/DMPO systems. Furthermore, the signals of HO• in the latter are much stronger than those in the former, indicating that the generation of HO• is greatly enhanced after adding Fe⁰@RF-C. In addition, the HO• signals are much stronger than $SO_4^{\bullet-}$, which may be attributed to the rapid transformation from DMPO-SO₄ adducts to DMPO-OH adducts [66]. No signals of DMPO−OOH are observed in the Fe⁰@RF-C/PS/DMPO system (Fig. 6b), indicating that $O_2^{\bullet-}$ is not generated in the system. The TEMPO signals (1:1:1) in the PS/TEMP system are attributed to the formation of $^1O_2$ due to the self-degradation of PS (Fig. 6c). These TEMPO signals are greatly enhanced in the Fe⁰@RF-C/PS/TEMP system, suggesting a significant generation of $^1O_2$ after the addition of Fe⁰@RF-C.

Although $SO_4^{\bullet-}$, HO•, and $^1O_2$ were detected in the EPR experiments, it does not necessarily mean that all of them are mainly
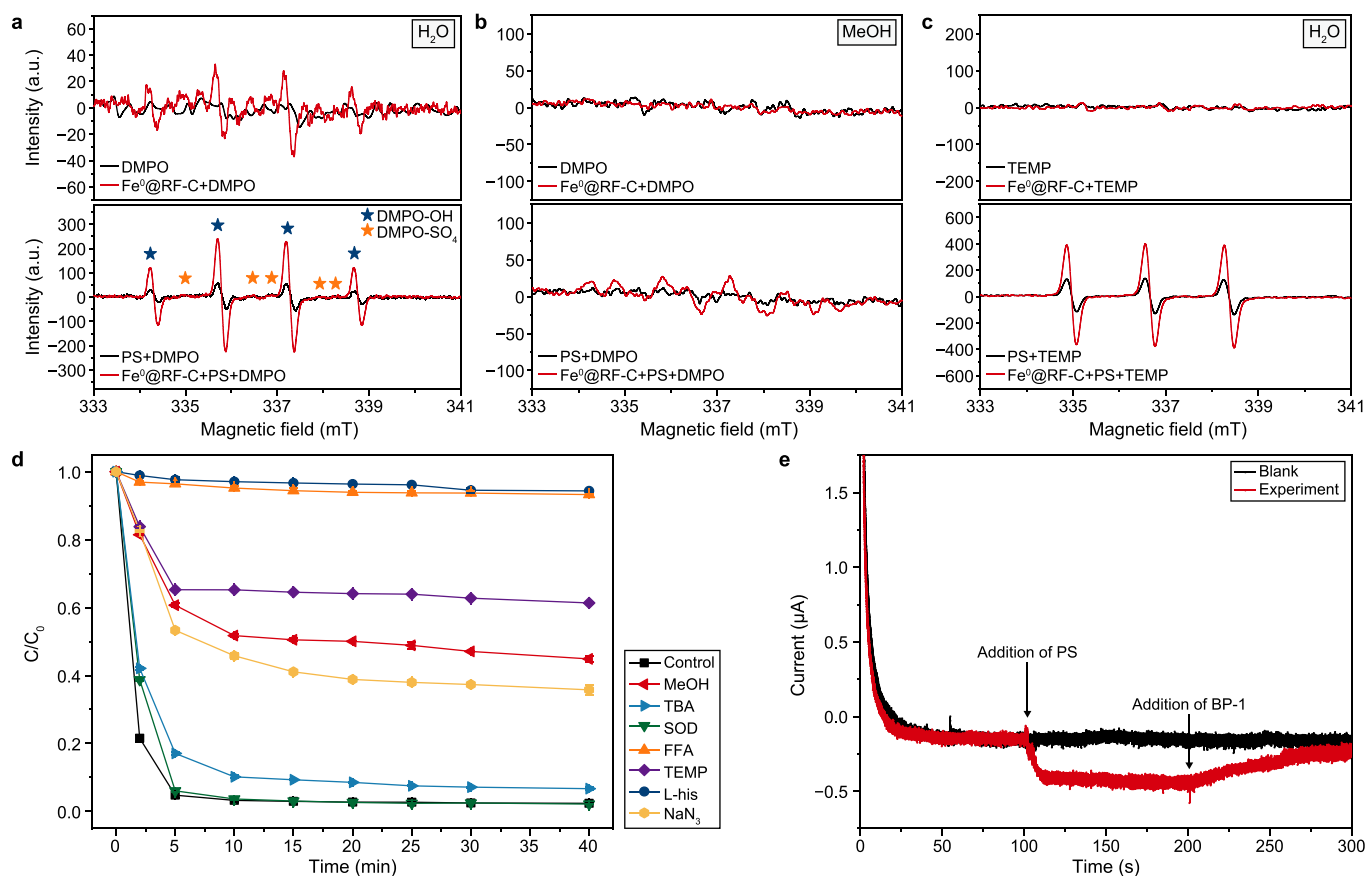
Fig. 6. a−b, EPR spectra obtained by spin trapping with 100 mmol L⁻¹ DMPO in water system (**a**) and MeOH system (**b**). **c**, EPR spectra obtained by spin trapping with 100 mmol L⁻¹ TEMP in the water system. **d**, Quenching experiments. **e**, Amperometric *i−t* curve measurements upon adding PS and BP-1 using Fe⁰@RF-C as the working electrode. Reaction conditions: [BP-1] = 20.0 μmol L⁻¹, [BP-1]:[PS] = 1:50, catalyst dosage = 50 mg L⁻¹, initial solution pH = 5.0 ± 0.1, T = 25.0 °C.

responsible for the degradation of BP-1. To further confirm the dominant active species, different quenchers were selected to investigate their effects on the degradation of BP-1, and the decomposition experiments of PS with and without the addition of these quenchers were also conducted. MeOH was selected to scavenge HO$^\bullet$ and SO$_4^{\bullet-}$ ($k_{\text{MeOH+HO}^\bullet}$ = 9.7 × 10^8 M^{-1} s^{-1}, $k_{\text{MeOH+SO}_4^{\bullet-}}$ = 2.5 × 10^7 M^{-1} s^{-1}), while TBA was used only to selectively quench HO$^\bullet$ ($k_{\text{TBA+HO}^\bullet}$ = (3.8−7.6) × 10^8 M^{-1} s^{-1}, $k_{\text{TBA+SO}_4^{\bullet-}}$ = (4.0−9.1) × 10^5 M^{-1} s^{-1}) [29]. SOD was used as a scavenger for O$_2^{\bullet-}$ [30]. FFA ($k_{\text{FFA+}^1\text{O}_2}$ = 1.2 × 10^8 M^{-1} s^{-1}) [67], L-his, and TEMP were used to quench ^{1}O$_2$. The addition of SOD (50000 U L^{-1}) shows almost no suppression in the removal of BP-1 (Fig. 6d), indicating that O$_2^{\bullet-}$ radicals hardly contribute to BP-1 degradation. Similarly, the addition of TBA (200 mmol L^{-1}) has a very weak inhibition on the degradation of BP-1, and TBA does not cause the decomposition of PS (Supplementary Material Fig. S7), indicating that the contribution of HO• radicals is very limited. On the contrary, adding MeOH (200 mmol L^{-1}) significantly inhibits the degradation of BP-1 but does not cause the decomposition of PS (Supplementary Material Fig. S7), indicating that SO$_4^{\bullet-}$ radicals play an important role in the degradation of BP-1.

Furthermore, we noticed that after adding MeOH, a considerable amount of BP-1 was still degraded, indicating the existence of non-radical pathways within the Fe^0@RF-C/PS system. To illustrate the contribution of ^{1}O$_2$, FFA, TEMP, and L-his, commonly used in the literature, were selected as scavengers to investigate their effects on the degradation of BP-1. TEMP (100 mmol L^{-1}) significantly inhibited the degradation of BP-1 (Fig. 6d). Particularly, the addition of FFA (100 mmol L^{-1}) and L-his (100 mmol L^{-1}) almost completely inhibited the degradation of BP-1. According to the literature [68], FFA can not only react with ^{1}O$_2$ but also quench HO$^\bullet$ and SO$_4^{\bullet-}$ radicals ($k_{\text{FFA+HO}^\bullet}$ = 1.5 × 10^{10} M^{-1} s^{-1}, $k_{\text{FFA+SO}_4^{\bullet-}}$ = 4.1 × 10^9 M^{-1} s^{-1}), therefore, it has a higher inhibitory effect on the removal of BP-1. Unfortunately, these three kinds of ^{1}O$_2$ scavengers led to significant decomposition of PS (Supplementary Material Fig. S7). Therefore, these quenching experiments could not accurately confirm the contribution of ^{1}O$_2$. For this reason, a low concentration of NaN$_3$ (2 mmol L^{-1}) was further used as a ^{1}O$_2$ scavenger. After adding a low concentration of NaN$_3$, the degradation of BP-1 was significantly inhibited, with less than 70% of BP-1 removed at 40 min (Fig. 6d). Although the addition of NaN$_3$ would also cause the decomposition of PS, more than 70% of PS (about 35 times the concentration of BP-1) was still retained in the system at 40 min (Supplementary Material Fig. S7). Combined with the result of PS concentration effect experiments (Fig. 5b), it was found that when the PS concentration was 25 times that of BP-
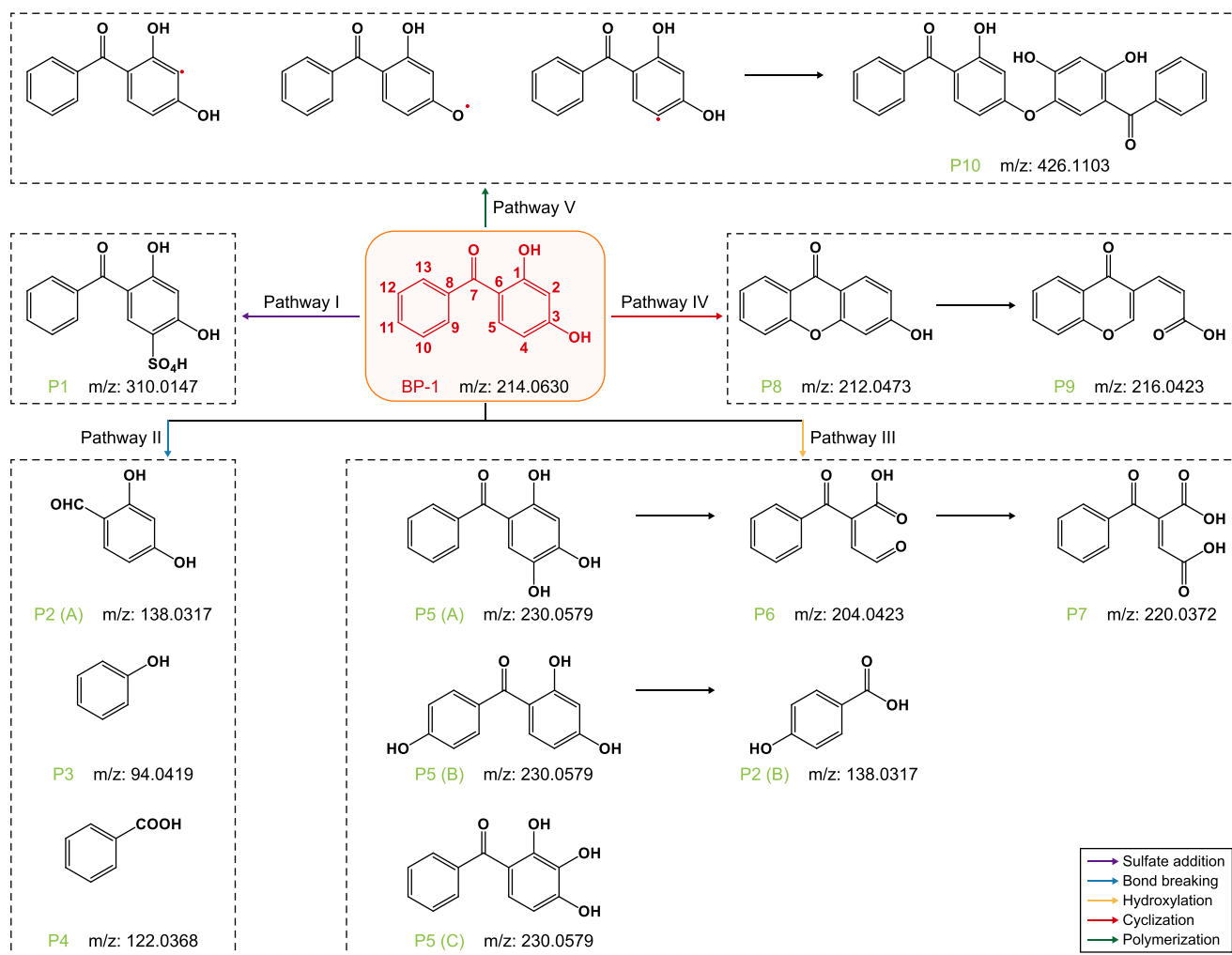

Fig. 7. Hypothetical degradation pathways of BP-1 in PS system activated by Fe^0@RF-C.

1, more than 90% of BP-1 could be removed within 40 min. Therefore, it can be considered inhibitory effect of NaN_3 on BP-1 degradation is mainly due to the quenching of $^1O_2$. According to previous studies, the generation of $^1O_2$ may be due to the activation of PS by graphitized carbon [69].

In addition to $^1O_2$, the direct electron transfer process mediated by graphite carbon is an important non-radical mechanism, often reported in advanced oxidation systems based on carbonaceous activators [70–72]. Thus, we hypothesized that BP-1 could also be degraded through an electron transfer process mediated by the carbon layer. Thereby, amperometric $i-t$ curves were recorded to monitor the charge transfer in the system. When PS was injected into the system, a negative current emerged immediately, whereas the addition of BP-1 resulted in an obvious signal of positive current (Fig. 6e). These observations indicate that the electrons can transfer from BP-1 to PS through a conductive graphitized carbon layer on Fe^0@RF-C surface, resulting in the decomposition of PS and the simultaneous degradation of BP-1 [72].

In summary, the $SO_4^{\bullet-}$ radicals and $^1O_2$ play a dominant role in BP-1 degradation, and the direct electron transfer from BP-1 to PS mediated by the graphitized carbon layer plays a secondary role, while the role of $HO\bullet$ radicals and $O_2^{\bullet-}$ is minor. Different from the conventional Fe^0 and PS-based oxidation process, where $SO_4^{\bullet-}$ and $HO^\bullet$ radicals play a major contribution to the degradation of pollutants, the Fe^0@RF-C/PS system can not only generate $SO_4^{\bullet-}$ radicals but also generate $^1O_2$ and can mediate the electron transfer from pollutants to PS, promoting the efficient degradation of pollutants through various ways. In addition, the enrichment of pollutants by the carbon layer is also conducive to their rapid degradation.

3.4. Oxidation intermediates and pathways

According to the LC-TOF-MS analysis, ten oxidation products were speculated during the degradation of BP-1. The errors between the experimental and calculated mass for all products were less than 5 ppm (Supplementary Material Table S3), indicating the high reliability of the structural identification. The MS/MS spectra were further used to analyze the oxidation products and their fragmentation patterns (Supplementary Material Fig. S8). Based on the analysis of oxidation products of BP-1 and previous reports [29,73,74], five possible pathways were proposed for the degradation of BP-1 in the mixed system of Fe^0@RF-C and PS (Fig. 7). In pathways I and III, the benzene ring of BP-1 was attacked by $SO_4^{\bullet-}$ and $HO^\bullet$, then the H atoms were easily substituted by them to generate their corresponding sulfate addition product P1 and hydroxylation product P5. P5 was further oxidized to form carboxylated products P2 (B), P6, and P7 through ring-opening or bond cleavage. The sulfate addition products and hydroxylation products have also been observed in previous studies on PS-based advanced oxidation processes [29,75]. In pathway II, $HO^\bullet$ could also attack the neighboring C atoms of carbonyl groups in BP-1 and cause bond cleavage to produce P2(A), P3, and P4. Moreover, in pathway IV, the BP-1 molecule was first attacked by free radicals ($SO_4^{\bullet-}$ and $HO^\bullet$) to generate a new free radical product with two single electrons, and a ring-closed product P8 was then formed through intramolecular coupling reactions, which was further oxidized to carboxylated product P9. Finally, in pathway V, BP-1 was first transformed into different radicals via electron extraction by $SO_4^{\bullet-}$ and $HO^\bullet$ and product P10 were formed through free radical coupling reactions. Other studies have also reported the coupling products [29,76].

3.5. The mineralization and toxicity changes

The TOC contents during the degradation process of BP-1 were

measured to evaluate the mineralization degree of BP-1. After adding PS, the TOC of the mixture solution sharply decreased to 68.8% within 2 min and then gradually stabilized to 58.4% after 40 min (Supplementary Material Fig. S9). This result indicates that most BP-1 was degraded into small intermediates in the oxidation process rather than completely mineralized into CO_2 and H_2O. Low TOC removal efficiencies have often been reported in other oxidation systems under mild conditions [29,77], indicating that further treatments are required to achieve complete mineralize pollutants.

To investigate changes in toxicity after the degradation of BP-1, the widely used ECOSAR program was selected to calculate the acute toxicity and chronic toxicity of BP-1 and its oxidation intermediates to fish, daphnia, and green algae (Supplementary Material Table S4). According to the global chemical classification system, the toxicity of chemicals can be divided into four levels: very toxic ($LC_{50}/EC_{50}/ChV \leq 1.0$ mg L^{-1}), toxic (1.0 mg L^{-1} < $LC_{50}/EC_{50}/ChV \leq 10.0$ mg L^{-1}), harmful (10.0 mg L^{-1} < $LC_{50}/EC_{50}/ChV \leq 100.0$ mg L^{-1}), and not harmful ($LC_{50}/EC_{50}/ChV > 100.0$ mg L^{-1}) [78]. The toxicity of BP-1 and its oxidation intermediates generated in pathways I–IV to fish was then plotted (Fig. 8). As can be seen, BP-1 is toxic to fish in terms of both acute toxicity and chronic toxicity. Under pathway I, product P1 shows lower toxicity than BP-
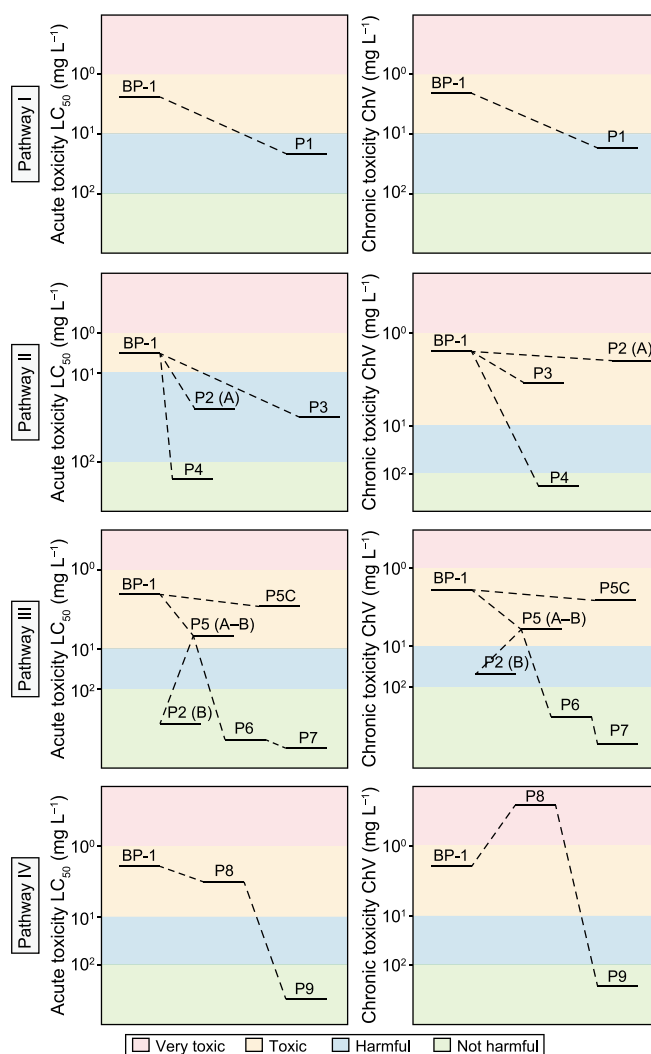

Fig. 8. Predicted aquatic toxicity of BP-1 and its degradation intermediates to fish by the ECOSAR program.

1 and is harmful to fish in acute and chronic toxicity. Under pathway II, P2(A) and P3 show lower toxicity than BP-1 and are harmful to fish in acute and chronic toxicity, whereas P4 is not harmful. Under pathway III, all the products, including P2(B), P5(A−C), P6, and P7, show prominently lower toxicity than BP-1 in acute and chronic toxicity, among which P6 and P7 are not harmful. Under pathway IV, although P8 shows higher toxicity than BP-1, its concentration is low and can be rapidly converted to P9, which is not harmful. Overall, the toxicity of the solution in the Fe^0@RF-C and PS mixed system decreased after the oxidative degradation of BP-1.

4. Conclusions

This study provided a simple and easy scale-up method to prepare carbon-coated nZVI composite, Fe^0@RF-C. Due to the protective effect of the carbon layer, Fe^0@RF-C showed higher air stability than commercial Fe^0. More importantly, the carbon layer promotes the enrichment of BP-1 on the surface of Fe^0@RF-C and introduces new oxidation mechanisms, including $^1O_2$ and direct electron transfer, which greatly enhances the degradation performance of the Fe^0@RF-C/PS system on BP-1 and improves its anti-interference ability against water background. This study offers valuable insights into the rational design of carbon-coated nZVI composites. It promotes the understanding of the crucial role of carbon layers in enhancing the catalytic performance of the composites, which is important for the practical application of ZVI. However, this study also has some shortcomings. For example, high temperature and a long calcination time are required to completely reduce Fe_3O_4 to Fe^0. It is possible to consider replacing Fe_3O_4 with Fe^0 to prepare carbon-coated nZVI composites by embedding methods.

Data availability

Data will be made available on request.

CRediT authorship contribution statement

Guizhou Xu: Writing - Review & Editing, Writing - Original Draft, Software, Methodology, Investigation, Formal Analysis, Conceptualization. **Lin Sun:** Writing - Review & Editing, Investigation, Formal Analysis. **Yizhou Tu:** Writing - Review & Editing, Methodology. **Xiaolei Teng:** Methodology, Data Curation. **Yumeng Qi:** Methodology, Data Curation. **Yaoyao Wang:** Methodology, Data Curation. **Aimin Li:** Writing - Review & Editing, Resources. **Xianchuan Xie:** Writing - Review & Editing, Validation, Supervision, Funding Acquisition, Conceptualization. **Xueyuan Gu:** Writing - Review & Editing, Validation, Supervision, Conceptualization.

Declaration of competing interest

The authors declare that they have no known competing financial interests or personal relationships that could have appeared to influence the work reported in this paper.

Acknowledgements

Appendix A. Supplementary data

Supplementary data to this article can be found online at https://doi.org/10.1016/j.ese.2024.100457.

References

[1] Y. Li, H.P. Zhao, L. Zhu, Remediation of soil contaminated with organic compounds by nanoscale zero-valent iron: a review, Sci. Total Environ. 760 (2021) 143413.

[2] Q. Li, Z. Chen, H. Wang, H. Yang, T. Wen, S. Wang, B. Hu, X. Wang, Removal of organic compounds by nanoscale zero-valent iron and its composites, Sci. Total Environ. 792 (2021) 148546.

[3] J. Xie, C. Lei, W. Chen, Q. Xie, Q. Guo, B. Huang, Catalytic properties of transition metals modified nanoscale zero-valent iron for simultaneous removal of 4-chlorophenol and Cr(VI): efficacy, descriptor and reductive mechanisms, J. Hazard Mater. 403 (2021) 123827.

[4] P. Fan, X. Zhang, H. Deng, X. Guan, Enhanced reduction of p-nitrophenol by zerovalent iron modified with carbon quantum dots, Appl. Catal. B Environ. 285 (2021).

[5] Y. Lü, J. Li, Y. Li, L. Liang, H. Dong, K. Chen, C. Yao, Z. Li, J. Li, X. Guan, The roles of pyrite for enhancing reductive removal of nitrobenzene by zero-valent iron, Appl. Catal. B Environ. 242 (2019) 9−18.

[6] D. Li, Y. Zhong, X. Zhu, H. Wang, W. Yang, Y. Deng, W. Huang, P. Peng, Reductive degradation of chlorinated organophosphate esters by nanoscale zerovalent iron/cetyltrimethylammonium bromide composites: reactivity, mechanism and new pathways, Water Res. 188 (2021) 116447.

[7] L.J. Xu, J.L. Wang, Degradation of chlorophenols using a novel Fe0/CeO2 composite, Appl. Catal. B Environ. 142−143 (2013) 396−405.

[8] S. Ahmad, X. Liu, J. Tang, S. Zhang, Biochar-supported nanosized zero-valent iron (nZVI/BC) composites for removal of nitro and chlorinated contaminants, Chem. Eng. J. 431 (2022).

[9] Y.W. Wu, X.T. Chen, Y. Han, D.T. Yue, X.D. Cao, Y.X. Zhao, X.F. Qian, Highly efficient utilization of nano-Fe(0) embedded in mesoporous carbon for activation of peroxydisulfate, Environ. Sci. Technol. 53 (15) (2019) 9081−9090.

[10] S. Zha, Y. Cheng, Y. Gao, Z. Chen, M. Megharaj, R. Naidu, Nanoscale zero-valent iron as a catalyst for heterogeneous Fenton oxidation of amoxicillin, Chem. Eng. J. 255 (2014) 141−148.

[11] H. Sun, G. Zhou, S. Liu, H.M. Ang, M.O. Tade, S. Wang, Nano-Fe(0) encapsulated in microcarbon spheres: synthesis, characterization, and environmental applications, ACS Appl. Mater. Interfaces 4 (11) (2012) 6235−6241.

[12] Y. Wang, H. Sun, X. Duan, H.M. Ang, M.O. Tadé, S. Wang, A new magnetic nano zero-valent iron encapsulated in carbon spheres for oxidative degradation of phenol, Appl. Catal. B Environ. 172−173 (2015) 73−81.

[13] Y. Dai, Y. Hu, B. Jiang, J. Zou, G. Tian, H. Fu, Carbothermal synthesis of ordered mesoporous carbon-supported nano zero-valent iron with enhanced stability and activity for hexavalent chromium reduction, J. Hazard Mater. 309 (2016) 249−258.

[14] S. Li, J. Tang, Q. Liu, X. Liu, B. Gao, A novel stabilized carbon-coated nZVI as heterogeneous persulfate catalyst for enhanced degradation of 4-chlorophenol, Environ. Int. 138 (2020) 105639.

[15] Z. Jiang, L. Lv, W. Zhang, Q. Du, B. Pan, L. Yang, Q. Zhang, Nitrate reduction using nanosized zero-valent iron supported by polystyrene resins: role of surface functional groups, Water Res. 45 (6) (2011) 2191−2198.

[16] Y.C. Lee, Y.F. Li, M.J. Chen, Y.C. Chen, J. Kuo, S.L. Lo, Efficient decomposition of perfluorooctanic acid by persulfate with iron-modified activated carbon, Water Res. 174 (2020) 115618.

[17] S.F. Jiang, L.L. Ling, W.J. Chen, W.J. Liu, D.C. Li, H. Jiang, High efficient removal of bisphenol A in a peroxymonosulfate/iron functionalized biochar system: mechanistic elucidation and quantification of the contributors, Chem. Eng. J. 359 (2019) 572−583.

[18] P. Su, W. Fu, X. Du, G. Song, M. Zhou, Confined Fe0@CNTs for highly efficient and super stable activation of persulfate in wide pH ranges: radicals and non-radical co-catalytic mechanism, Chem. Eng. J. 420 (2021).

[19] M. Liu, N. Wu, B. Tian, D. Zhou, C. Yan, Z. Huo, R. Qu, Experimental and theoretical study on the degradation of Benzophenone-1 by Ferrate(VI): new insights into the oxidation mechanism, J. Hazard Mater. 425 (2022) 127877.

[20] C.J. Gao, L.Y. Liu, W.L. Ma, N.Z. Zhu, L. Jiang, Y.F. Li, K. Kannan, Benzonphenone-type UV filters in urine of Chinese young adults: concentration, source and exposure, Environ. Pollut. 203 (2015) 1−6.

[21] R. Rodriguez-Gomez, A. Zafra-Gomez, F.J. Camino-Sanchez, O. Ballesteros, A. Navalon, Gas chromatography and ultra high performance liquid chromatography tandem mass spectrometry methods for the determination of selected endocrine disrupting chemicals in human breast milk after stir-bar sorptive extraction, J. Chromatogr. A 1349 (2014) 69−79.

[22] B. Zhang, J.J. Ruan, L. Xie, M.W. Gui, X.Y. Bai, T. Zhang, Urinary benzophenone-type UV filters in people living in South China: rural versus urban areas, Environ Sci Process Impacts 20 (3) (2018) 553−560.

[23] T. Zhang, H. Sun, X. Qin, Q. Wu, Y. Zhang, J. Ma, K. Kannan, Benzophenone-

type UV filters in urine and blood from children, adults, and pregnant women in China: partitioning between blood and urine as well as maternal and fetal cord blood, Sci. Total Environ. 461−462 (2013) 49−55.

[24] M.M. Tsui, H.W. Leung, T.C. Wai, N. Yamashita, S. Taniyasu, W. Liu, P.K. Lam, M.B. Murphy, Occurrence, distribution and ecological risk assessment of multiple classes of UV filters in surface waters from different countries, Water Res. 67 (2014) 55−65.

[25] M.M. Tsui, H.W. Leung, P.K. Lam, M.B. Murphy, Seasonal occurrence, removal efficiencies and preliminary risk assessment of multiple classes of organic UV filters in wastewater treatment plants, Water Res. 53 (2014) 58−67.

[26] K. Morohoshi, H. Yamamoto, R. Kamata, F. Shiraishi, T. Koda, M. Morita, Estrogenic activity of 37 components of commercial sunscreen lotions evaluated by in vitro assays, Toxicol. Vitro 19 (4) (2005) 457−469.

[27] S. Kim, K. Choi, Occurrences, toxicities, and ecological risks of benzophenone-3, a common component of organic sunscreen products: a mini-review, Environ. Int. 70 (2014) 143−157.

[28] M.A. Park, K.A. Hwang, H.R. Lee, B.R. Yi, E.B. Jeung, K.C. Choi, Benzophenone-1 stimulated the growth of BG-1 ovarian cancer cells by cell cycle regulation via an estrogen receptor alpha-mediated signaling pathway in cellular and xenograft mouse models, Toxicology 305 (2013) 41−48.

[29] M. Zou, Y. Qi, R. Qu, G. Al-Basher, X. Pan, Z. Wang, Z. Huo, F. Zhu, Effective degradation of 2,4-dihydroxybenzophenone by zero-valent iron powder (Fe(0))-activated persulfate in aqueous solution: kinetic study, product identification and theoretical calculations, Sci. Total Environ. 771 (2021) 144743.

[30] W. Ren, C. Cheng, P. Shao, X. Luo, H. Zhang, S. Wang, X. Duan, Origins of electron-transfer regime in persulfate-based nonradical oxidation processes, Environ. Sci. Technol. 56 (1) (2021) 78−97.

[31] T. Zhang, H.B. Zhu, J.P. Croue, Production of sulfate radical from peroxymonosulfate induced by a magnetically separable CuFe2O4 spinel in water: efficiency, stability, and mechanism, Environ. Sci. Technol. 47 (6) (2013) 2784−2791.

[32] J. Kim, G.N. Coulibaly, S. Yoon, A.A. Assadi, K. Hanna, S. Bae, Red mud-activated peroxymonosulfate process for the removal of fluoroquinolones in hospital wastewater, Water Res. 184 (2020) 116171.

[33] G.N. Coulibaly, S. Bae, J. Kim, A.A. Assadi, K. Hanna, Enhanced removal of antibiotics in hospital wastewater by Fe−ZnO activated persulfate oxidation, Environ. Sci. J. Integr. Environ. Res.: Water Research & Technology 5 (12) (2019) 2193−2201.

[34] M. Kamagate, A.A. Assadi, T. Kone, S. Giraudet, L. Coulibaly, K. Hanna, Use of laterite as a sustainable catalyst for removal of fluoroquinolone antibiotics from contaminated water, Chemosphere 195 (2018) 847−853.

[35] C. Liang, C.F. Huang, N. Mohanty, R.M. Kurakalva, A rapid spectrophotometric determination of persulfate anion in ISCO, Chemosphere 73 (9) (2008) 1540−1543.

[36] H. Lv, H. Niu, X. Zhao, Y. Cai, F. Wu, Carbon zero-valent iron materials possessing high-content fine Fe0 nanoparticles with enhanced microelectrolysis-Fenton-like catalytic performance for water purification, Appl. Catal. B Environ. 286 (2021).

[37] X.X. Pan, J. Chen, N.N. Wu, Y.M. Qi, X.X. Xu, J.L. Ge, X.H. Wang, C.G. Li, R.J. Qu, V.K. Sharma, Z.Y. Wang, Degradation of aqueous 2,4,4 '-Trihydroxybenzophenone by persulfate activated with nitrogen doped carbonaceous materials and the formation of dimer products, Water Res. 143 (2018) 176−187.

[38] X.L. Zhang, M.B. Feng, R.J. Qu, H. Liu, L.S. Wang, Z.Y. Wang, Catalytic degradation of diethyl phthalate in aqueous solution by persulfate activated with nano-scaled magnetic CuFe2O4/MWCNTs, Chem. Eng. J. 301 (2016) 1−11.

[39] Y. Gao, Q. Wang, G. Ji, A. Li, Degradation of antibiotic pollutants by persulfate activated with various carbon materials, Chem. Eng. J. 429 (2022).

[40] J. Lee, U. von Gunten, J.H. Kim, Persulfate-based advanced oxidation: critical assessment of opportunities and roadblocks, Environ. Sci. Technol. 54 (6) (2020) 3064−3081.

[41] Y. Zhang, B.T. Zhang, Y. Teng, J. Zhao, X. Sun, Heterogeneous activation of persulfate by carbon nanofiber supported Fe3O4@carbon composites for efficient ibuprofen degradation, J. Hazard Mater. 401 (2021) 123428.

[42] Y. Yan, H. Zhang, W. Wang, W. Li, Y. Ren, X. Li, Synthesis of Fe(0)/Fe3O4@ porous carbon through a facile heat treatment of iron-containing candle soots for peroxymonosulfate activation and efficient degradation of sulfamethoxazole, J. Hazard Mater. 411 (2021) 124952.

[43] Y. Yang, W. Ji, X. Li, H. Lin, H. Chen, F. Bi, Z. Zheng, J. Xu, X. Zhang, Insights into the mechanism of enhanced peroxymonosulfate degraded tetracycline using metal organic framework derived carbonyl modified carbon-coated Fe(0), J. Hazard Mater. 424 (Pt D) (2022) 127640.

[44] R.T. Mayes, P.F. Fulvio, Z. Ma, S. Dai, Phosphorylated mesoporous carbon as a solid acid catalyst, Phys. Chem. Chem. Phys. 13 (7) (2011) 2492−2494.

[45] Y. Zhang, B.T. Zhang, Y.G. Teng, J.J. Zhao, Activated carbon supported nanoscale zero valent iron for cooperative adsorption and persulfate-driven oxidation of ampicillin, Environ. Technol. Innovat. 19 (2020) 100956.

[46] J.H. Chen, X.L. Yu, C. Li, X. Tang, Y. Sun, Removal of tetracycline via the synergistic effect of biochar adsorption and enhanced activation of persulfate, Chem. Eng. J. 382 (2020) 122916.

[47] S.S. Zhu, X.C. Huang, F. Ma, L. Wang, X.G. Duan, S.B. Wang, Catalytic removal of aqueous contaminants on N-doped graphitic biochars: inherent roles of adsorption and nonradical mechanisms, Environ. Sci. Technol. 52 (15) (2018) 8649−8658.

[48] Y. Qi, B. Ge, Y. Zhang, B. Jiang, C. Wang, M. Akram, X. Xu, Three-dimensional porous graphene-like biochar derived from Enteromorpha as a persulfate activator for sulfamethoxazole degradation: role of graphitic N and radicals transformation, J. Hazard Mater. 399 (2020) 123039.

[49] J.F. Yu, L. Tang, Y. Pang, G.M. Zeng, J.J. Wang, Y.C. Deng, Y.N. Liu, H.P. Feng, S. Chen, X.Y. Ren, Magnetic nitrogen-doped sludge-derived biochar catalysts for persulfate activation: internal electron transfer mechanism, Chem. Eng. J. 364 (2019) 146−159.

[50] Y. Wu, X. Chen, Y. Han, D. Yue, X. Cao, Y. Zhao, X. Qian, Highly efficient utilization of nano-Fe(0) embedded in mesoporous carbon for activation of peroxydisulfate, Environ. Sci. Technol. 53 (15) (2019) 9081−9090.

[51] K. Zhu, H. Xu, C. Chen, X. Ren, A. Alsaedi, T. Hayat, Encapsulation of Fe0-dominated Fe3O4/Fe0/Fe3C nanoparticles into carbonized polydopamine nanospheres for catalytic degradation of tetracycline via persulfate activation, Chem. Eng. J. 372 (2019) 304−311.

[52] C. Liang, Z.S. Wang, C.J. Bruell, Influence of pH on persulfate oxidation of TCE at ambient temperatures, Chemosphere 66 (1) (2007) 106−113.

[53] M. Amasha, A. Baalbaki, A. Ghauch, A comparative study of the common persulfate activation techniques for the complete degradation of an NSAID: the case of ketoprofen, Chem. Eng. J. 350 (2018) 395−410.

[54] A. Ghauch, G. Ayoub, S. Naim, Degradation of sulfamethoxazole by persulfate assisted micrometric Fe0 in aqueous solution, Chem. Eng. J. 228 (2013) 1168−1181.

[55] H.X. Liu, J.Y. Yao, L.H. Wang, X.H. Wang, R.J. Qu, Z.Y. Wang, Effective degradation of fenitrothion by zero-valent iron powder (Fe-0) activated persulfate in aqueous solution: kinetic study and product identification, Chem. Eng. J. 358 (2019) 1479−1488.

[56] J.F. Yang, L.M. Yang, S.B. Zhang, L.H. Ou, C.B. Liu, L.Y. Zheng, Y.F. Yang, G.G. Ying, S.L. Luo, Degradation of azole fungicide fluconazole in aqueous solution by thermally activated persulfate, Chem. Eng. J. 321 (2017) 113−122.

[57] D. Miao, J. Peng, X. Zhou, L. Qian, M. Wang, L. Zhai, S. Gao, Oxidative degradation of atenolol by heat-activated persulfate: kinetics, degradation pathways and distribution of transformation intermediates, Chemosphere 207 (2018) 174−182.

[58] X.-R. Xu, X.-Z. Li, Degradation of azo dye Orange G in aqueous solutions by persulfate with ferrous ion, Separ. Purif. Technol. 72 (1) (2010) 105−111.

[59] M. Xu, X. Gu, S. Lu, Z. Qiu, Q. Sui, Z. Miao, X. Zang, X. Wu, Degradation of carbon tetrachloride in aqueous solution in the thermally activated persulfate system, J. Hazard Mater. 286 (2015) 7−14.

[60] Y. Chen, P. Deng, P. Xie, R. Shang, Z. Wang, S. Wang, Heat-activated persulfate oxidation of methyl- and ethyl-parabens: effect, kinetics, and mechanism, Chemosphere 168 (2017) 1628−1636.

[61] M. Zou, Y. Qi, R. Qu, G. Al-Basher, X. Pan, Z. Wang, Z. Huo, F. Zhu, Effective degradation of 2,4-dihydroxybenzophenone by zero−valent iron powder (Fe0)-activated persulfate in aqueous solution: kinetic study, product identification and theoretical calculations, Sci. Total Environ. 771 (2021).

[62] S.L. Wang, J.F. Wu, X.Q. Lu, W.X. Xu, Q. Gong, J.Q. Ding, B.S. Dan, P.C. Xie, Removal of acetaminophen in the Fe2+/persulfate system: kinetic model and degradation pathways, Chem. Eng. J. 358 (2019) 1091−1100.

[63] Y.F. Rao, L. Qu, H. Yang, W. Chu, Degradation of carbamazepine by Fe(II)-activated persulfate process, J. Hazard Mater. 268 (2014) 23−32.

[64] L. Zheng, H. Su, J. Zhang, L.S. Walekar, H. Vafaei Molamahmood, B. Zhou, M. Long, Y.H. Hu, Highly selective photocatalytic production of H2O2 on sulfur and nitrogen co-doped graphene quantum dots tuned TiO2, Appl. Catal. B Environ. 239 (2018) 475−484.

[65] I.A. Katsoyiannis, T. Ruettimann, S.J. Hug, pH dependence of Fenton reagent generation and As(III) oxidation and removal by corrosion of zero valent iron in aerated water, Environ. Sci. Technol. 42 (19) (2008) 7424−7430.

[66] Z. Wang, J. Jiang, S. Pang, Y. Zhou, C. Guan, Y. Gao, J. Li, Y. Yang, W. Qiu, C. Jiang, Is sulfate radical really generated from peroxydisulfate activated by iron(II) for environmental decontamination? Environ. Sci. Technol. 52 (19) (2018) 11276−11284.

[67] C. Dai, S. Li, Y. Duan, K.H. Leong, S. Liu, Y. Zhang, L. Zhou, Y. Tu, Mechanisms and product toxicity of activated carbon/peracetic acid for degradation of sulfamethoxazole: implications for groundwater remediation, Water Res 216 (2022) 118347.

[68] Z.-H. Xie, C.-S. He, D.-N. Pei, Y. Dong, S.-R. Yang, Z. Xiong, P. Zhou, Z.-C. Pan, G. Yao, B. Lai, Review of characteristics, generation pathways and detection methods of singlet oxygen generated in advanced oxidation processes (AOPs), Chem. Eng. J. 468 (2023).

[69] X. Cheng, H.G. Guo, Y.L. Zhang, X. Wu, Y. Liu, Non-photochemical production of singlet oxygen via activation of persulfate by carbon nanotubes, Water Res. 113 (2017) 80−88.

[70] C. Zhao, L. Meng, H. Chu, J.-F. Wang, T. Wang, Y. Ma, C.-C. Wang, Ultrafast degradation of emerging organic pollutants via activation of peroxymonosulfate over Fe3C/Fe@N-C-x: singlet oxygen evolution and electron-transfer mechanisms, Appl. Catal. B Environ. 321 (2023).

[71] H. Lee, H.I. Kim, S. Weon, W. Choi, Y.S. Hwang, J. Seo, C. Lee, J.H. Kim, Activation of persulfates by graphitized nanodiamonds for removal of organic compounds, Environ. Sci. Technol. 50 (18) (2016) 10134−10142.

[72] P.H. Shao, S.P. Yu, X.G. Duan, L.M. Yang, H. Shi, L. Ding, J.Y. Tian, L.X. Yang, X.B. Luo, S.B. Wang, Potential difference driving electron transfer via defective carbon nanotubes toward selective oxidation of organic micropollutants, Environ. Sci. Technol. 54 (13) (2020) 8464−8472.

[73] P. Sun, H. Liu, Z.C. Zhai, X.S. Zhang, Y.S. Fang, J. Tan, J.Q. Wu, Degradation of UV

filter BP-1 with nitrogen-doped industrial graphene as a metal-free catalyst of peroxymonosulfate activation, Chem. Eng. J. 356 (2019) 262−271.

[74] J. Ge, D. Huang, Z. Han, X. Wang, X. Wang, Z. Wang, Photochemical behavior of benzophenone sunscreens induced by nitrate in aquatic environments, Water Res. 153 (2019) 178−186.

[75] L.J. Xu, W. Chu, L. Gan, Environmental application of graphene-based CoFe2O4 as an activator of peroxymonosulfate for the degradation of a plasticizer, Chem. Eng. J. 263 (2015) 435−443.

[76] J. Ge, D. Huang, Z. Han, X. Wang, X. Wang, Z. Wang, Photochemical behavior of benzophenone sunscreens induced by nitrate in aquatic environments, Water Res. 153 (2019) 178−186.

[77] H. Liu, P. Sun, M.B. Feng, H.X. Liu, S.G. Yang, L.S. Wang, Z.Y. Wang, Nitrogen and sulfur co-doped CNT-COOH as an efficient metal-free catalyst for the degradation of UV filter BP-4 based on sulfate radicals, Appl. Catal. B Environ. 187 (2016) 1−10.

[78] S. Kadam, Globally harmonized system of classification and labeling of chemicals, Chem. Eng. World 45 (5) (2010) 46−49.